

Numerical study of staggered quark action on quenched anisotropic lattices

Kouji NOMURA^{1,*}, Hideo MATSUFURU^{2,**}, and Takashi UMEDA^{3,***},

¹*Department of Physics, Hiroshima University,
Higashi-hiroshima 739-8626, Japan*

²*Computing Research Center, High Energy Accelerator Research Organization
(KEK), Tsukuba 305-0801, Japan*

³*Yukawa Institute for Theoretical Physics, Kyoto University,
Kyoto 606-8502, Japan*

The staggered quark action on anisotropic lattices is studied. We carry out numerical simulations in the quenched approximation at three values of lattice spacing ($a_\sigma^{-1} = 1 - 2$ GeV) with the anisotropy $\xi = a_\sigma/a_\tau = 4$, where a_σ and a_τ are the spatial and temporal lattice spacings, respectively. The bare anisotropy γ_F in the quark action is numerically tuned through the ratio of meson masses in the fine and coarse directions, and through the dispersion relation of a meson, so that the renormalized fermionic anisotropy coincides with that of the gauge field. The discrepancy between these two calibration schemes provides an estimate of the finite lattice artifact, which is found to be sizable in the range of cutoff explored in this work. We also compute the meson masses using correlators with the wall source at the tuned anisotropy parameter. The flavor symmetry breaking effect smoothly decreases as β increases. The effect of uncertainty in γ_F on the meson masses are examined. We also discuss a perspective on dynamical simulations.

§1. Introduction

In numerical studies of lattice QCD, one frequently encounters a case which requires a fine lattice spacing in the temporal direction while does not comparatively in the spatial directions. Increasing the lattice cutoffs in all the four directions severely increases the computational cost, since it increases at least in proportion to the volume of the lattice, and in fact more rapidly in particular in dynamical simulations.¹⁾ A solution is provided by anisotropic lattices,²⁾ on which the temporal lattice spacing is finer than the spatial ones. The technique is useful in various fields of the lattice QCD simulation: At finite temperature, a large number of the degrees of freedom in the Euclidean time direction leads a large number of Matsubara frequencies, which is efficient for calculations of the equation of state³⁾ and for analyses of temporal correlation functions of hadrons.^{4)–8)} The large temporal cutoff is important for relativistic formulations of heavy quark on the lattice.^{9)–13)} It is also efficient when the signal-to-noise ratio deteriorate quickly, as in the cases of glueballs,^{6),14)} negative parity baryons,¹⁵⁾ and the pion scattering length.¹⁶⁾

On the other hand, on anisotropic lattices one has additional parameters in

*) E-mail: nomura1@hiroshima-u.ac.jp

**) E-mail: hideo.matsufuru@kek.jp

***) E-mail: tumeda@yukawa.kyoto-u.ac.jp

the actions which control the anisotropies of the fields. In general these anisotropy parameters should be tuned numerically. Inappropriate tuning of the parameters breaks the rotational symmetry of the lattice, and may lead unphysical results. The uncertainties in the tuning of the parameters bring additional errors into observed quantities. For precise calculations, one needs to tune anisotropy parameters with good statistical accuracy and to control the systematic errors in the continuum extrapolation. In this paper, we investigate this calibration process in detail for the staggered quark action.

To explain the situation we are faced with in more detail, let us focus on a study of hadrons at finite temperature, which is a main motivation of present work. To investigate the hadron structure at $T > 0$, one needs to treat the hadron correlators in the temporal direction.^{4),5),17)} Because the lattice size in the temporal direction is limited to $N_t a_\tau = 1/T$, where T is the temperature, near and above the critical temperature the number of degrees of freedom is severely limited without introducing the anisotropic lattice. For example, the number of degrees of freedom is significant for reliable extraction of the spectral function from the lattice data.^{7),8),18)}

So far the studies of hadrons at finite temperature have been performed mainly on quenched lattices. Dynamical simulations are manifestly important, as exhibited by the fact that the order of phase transition changes as the number of dynamical quark flavors varies. As the quark action we adopt the staggered action, which has several advantages over the Wilson-type quarks:¹⁹⁾ Firstly, the staggered action retains the remnant of the chiral symmetry. This is important to investigate the role of the chiral symmetry near the phase transition. Secondly, one can explore smaller quark mass region than the cases with the Wilson-type formulations. Thirdly, the cost of numerical simulation is much more economical than the other formulations. A disadvantage lies in its complication in the flavor structure. To circumvent the effects of the flavor symmetry breaking, improved versions of the staggered fermion have been developed.

In this work, however, we adopt the simplest version without any improvement. This is because an improvement adds the anisotropy parameters which is to be tuned in general nonperturbatively. At this first stage of development of the anisotropic staggered action, we concentrate on the most significant effect of the anisotropy on the spectrum. For the gauge field we adopt the standard Wilson plaquette action, which has the discretization errors in the same order as the quark action we adopt. The same combination of actions have also been used in Ref.²⁰⁾ for a dynamical simulation, while their discussion on the systematic errors and statistical precision were not sufficient for our present purposes.

The dynamical anisotropic lattices are more involved than the quenched case, since one needs to tune the anisotropy parameters for the gauge and quark fields simultaneously. So far there is no systematic investigation of anisotropic staggered quarks even in the quenched approximation. In this paper we therefore concentrate on the quenched approximation and investigate the properties of the staggered quark on anisotropic lattices.

The numerical simulations are performed on quenched lattices with three lattice spacings, at fixed renormalized anisotropy $\xi = 4$. These scales cover the range of the

spatial lattice cutoff $a_\sigma^{-1} = 1 - 2$ GeV. We apply two calibration procedures with different definitions of fermionic anisotropy ξ_F : with the ratio of the masses in the fine and coarse directions, and through the meson dispersion relation. The former has an advantage in statistical precision, while the latter can be used even in the heavy quark mass region. Differences between the results of these two procedures signal the finite lattice artifacts. For the reason of statistical fluctuations, we use only the pseudoscalar channel in the calibration. Other mesonic channels are observed in the second part of the paper by employing the wall source, and compared with the results on the isotropic lattices.

This paper is organized as follows. The next section briefly summarizes the anisotropic staggered action. Section 3 describes the calibration procedures. The numerical result of the calibration is presented in Sec. 4. Section 5 describes the spectroscopy with the wall source. Section 6 is devoted to our conclusions in the quenched simulations. In the last section, we give our perspective toward the dynamical simulations with the staggered quarks.

§2. Staggered quark on anisotropic lattices

2.1. Anisotropic lattice actions

The gauge field is described with the standard Wilson gauge action,

$$S_G = \beta \sum_x \left\{ \sum_{i < j=1}^3 \frac{1}{\gamma_G} \left[1 - \frac{1}{3} \text{Re Tr } U_{ij}(x) \right] + \sum_{i=1}^3 \gamma_G \left[1 - \frac{1}{3} \text{Re Tr } U_{i4}(x) \right] \right\}, \quad (2.1)$$

where $\beta = 6/g_0^2$ is the bare coupling and γ_G the bare gauge anisotropy parameter. The plaquette variable $U_{\mu\nu}(x)$ is defined with the link variable $U_\mu(x) \simeq e^{ig a_\mu A_\mu(x)} \in \text{SU}(3)$ as

$$U_{\mu\nu}(x) = U_\mu(x) U_\nu(x + \hat{\mu}) U_\mu^\dagger(x + \hat{\nu}) U_\nu^\dagger(x). \quad (2.2)$$

A lattice site is labeled by an integer vector x whose component x_μ is in units of lattice spacing a_μ , where $a_1 = a_2 = a_3 = a_\sigma$ and $a_4 = a_\tau$. $\hat{\mu}$ is a unit vector in the μ -th direction.

The staggered quark action on an anisotropic lattice is defined as

$$S_F = \sum_{x,y} \bar{\chi}(x) K(x,y) \chi(y), \quad (2.3)$$

$$K(x,y) = \delta_{x,y} - \kappa_\sigma \sum_{i=1}^3 \eta_i(x) \left[U_i(x) \delta_{x+\hat{i},y} - U_i^\dagger(x - \hat{i}) \delta_{x-\hat{i},y} \right] \\ - \gamma_F \kappa_\sigma \eta_4(x) \left[U_4(x) \delta_{x+\hat{4},y} - U_4^\dagger(x - \hat{4}) \delta_{x-\hat{4},y} \right], \quad (2.4)$$

where γ_F is the bare anisotropy of the quark field, $\kappa_\sigma = 1/2m_q$ with m_q the bare quark mass in spatial lattice units. $\eta_\mu(x)$ is the staggered phase, $\eta_\mu(x) = (-1)^{x_1 + \dots + x_{\mu-1}}$, with $\eta_1(x) = 1$.

The staggered quark fields χ and $\bar{\chi}$ have only the color components. The 4-spinor field with four degenerate flavors, $\psi_\alpha^f(X)$, where X labels the space-time position in units of $2a_\mu$, are represented as a linear combination of $\chi(x)$ as^{21), 22)}

$$\psi_\alpha^f(X) = \frac{1}{\sqrt{2}} \sum_\rho (T_\rho)_{\alpha f} \chi_\rho(X), \quad (2.5)$$

$$T_\rho = \gamma_1^{\rho_1} \gamma_2^{\rho_2} \gamma_3^{\rho_3} \gamma_4^{\rho_4}, \quad (2.6)$$

$$\chi_\rho(X) = \chi(2X + \rho), \quad (2.7)$$

where ρ labels a position in the hypercube and its components are 0 or 1. Therefore the quantum number of a quark bilinear is specified by its spin-flavor structure.^{22), 23)}

2.2. Meson correlators

The meson correlators are composed of the quark propagator,

$$S(x, y) = \langle \chi(x) \bar{\chi}(y) \rangle = K^{-1}(x, y), \quad (2.8)$$

which is obtained by solving a linear equation

$$\sum_x K(z, x) S(x, 0) = b(\vec{z}) \delta_{z_4, 0}, \quad (2.9)$$

where the vector $b(\vec{z})$ is a source field. (The color index is omitted.) As $b(\vec{z})$, we select the following two cases; (i) the point source, $b_p(\vec{y}) = \delta_{\vec{y}, 0}$, and (ii) the wall sources, $b_e(\vec{y}) = 1$ and $b_o(\vec{y}) = (-1)^{y_1 + y_2 + y_3}$. In the latter case, the gauge must be fixed.

In this paper, we treat single time-slice correlators, namely the sink operators at each t are defined only in a spatial plane on a single time slice.²⁴⁾ Such a correlator contains two modes, one monotonously and the other oscillatingly decay. The latter has the opposite parity to the former. In the following, the correlators are labeled by their non-oscillating channels.

The meson correlators composed of the quark propagator with the point source are used in the calibration (Sec. 4). Since we do not fix the gauge at this stage, the correlators must be constructed with the gauge invariant ingredients. The pseudoscalar and vector correlators are represented as

$$M_{PS}(t) = \sum_{\vec{x}} |S_p(x)|^2, \quad (2.10)$$

$$M_{V_j}(t) = \sum_{\vec{x}} (-)^{x_j} |S_p(x)|^2 \quad (j = 1, 2, 3), \quad (2.11)$$

where $S_p(x)$ is the quark propagator with the point source at the origin. These correlators have spin-flavor structures $\gamma_5 \otimes \gamma_5$ and $\gamma_j \otimes \gamma_j$, respectively. While these representations are for the vanishing meson momentum, the momentum insertion is straightforward. In the case of vector correlator, the finite momentum state needs some care, since the operator mixes with the fourth component. However we do not discuss this problem further, since we decide to use only the pseudoscalar correlator

in the calibration because of large fluctuation in the vector channel. We also measure the correlators in the z -direction to define the anisotropy through the ratio of masses in the fine and coarse directions. Rewriting Eqs. (2.10) and (2.11) for the correlators in z -direction is also straightforward.

The correlators composed of the quark propagators with wall sources are as follows.²⁵⁾

$$M_\pi(t) = \sum_{\vec{x}} \left[S_e^\dagger(x) S_e(x) + S_o^\dagger(x) S_o(x) \right] \quad (2.12)$$

$$M_{\tilde{\pi}}(t) = \sum_{\vec{x}} (-)^{x_1+x_2+x_3} \left[S_e^\dagger(x) S_o(x) + S_o^\dagger(x) S_e(x) \right] \quad (2.13)$$

$$M_{\pi_3}(t) = \sum_{\vec{x}} \left[S_e^\dagger(x + \hat{3}) S_e(x) - S_o^\dagger(x + \hat{3}) S_o(x) \right] \quad (2.14)$$

$$M_{\tilde{\pi}_3}(t) = \sum_{\vec{x}} (-)^{x_1+x_2+x_3} \left[S_e^\dagger(x + \hat{3}) S_o(x) - S_o^\dagger(x + \hat{3}) S_e(x) \right] \quad (2.15)$$

$$M_{\rho_6^A}(t) = \sum_{\vec{x}} \left[S_e^\dagger(x + \hat{2} + \hat{3}) S_e(x) + S_o^\dagger(x + \hat{2} + \hat{3}) S_o(x) \right] \quad (2.16)$$

$$M_{\rho_6^B}(t) = \sum_{\vec{x}} (-)^{x_1+x_2+x_3} \left[S_e^\dagger(x + \hat{2} + \hat{3}) S_o(x) + S_o^\dagger(x + \hat{2} + \hat{3}) S_e(x) \right] \quad (2.17)$$

The spin-flavor structures of these correlators are; π : $\gamma_5 \otimes \gamma_5$, $\tilde{\pi}$: $\gamma_4\gamma_5 \otimes \gamma_4\gamma_5$, π_3 : $\gamma_5 \otimes \gamma_5\gamma_3$, $\tilde{\pi}_3$: $\gamma_4\gamma_5 \otimes \gamma_4\gamma_5\gamma_3$, ρ_6^A : $\gamma_3 \otimes \gamma_2$, and ρ_6^B : $\gamma_3\gamma_4 \otimes \gamma_2\gamma_4$. In addition to these quantum numbers, each correlator contains the opposite parity channel as the oscillating mode. The correlator (2.12) has the same quantum number as Eq. (2.10). On the other hand, the quantum number of the correlators (2.16) and (2.17) are different from that of Eq. (2.11) at finite lattice spacing.

At large t , the correlator approaches a form²⁴⁾

$$M(t) \rightarrow Z \exp(-mt) + (-)^t \tilde{Z} \exp(-\tilde{m}t). \quad (2.18)$$

To extract the meson masses, we fit the numerical data of the meson correlator with the wall source to this form after adding the contribution via the temporal boundary. In the calibration, only the first term in Eq. (2.18) is retained since the contribution from the second term quickly disappears in the pseudoscalar channel.

§3. Calibration procedures

3.1. Calibration schemes

The anisotropy parameters γ_G and γ_F should be tuned so that the physical isotropy condition, $\xi_G(\gamma_G^*, \gamma_F^*) = \xi_F(\gamma_G^*, \gamma_F^*) = \xi$, holds at each set of β and m_q , where $\xi_G(\gamma_G, \gamma_F)$ and $\xi_F(\gamma_G, \gamma_F)$ are the renormalized anisotropies defined through the gauge and fermionic observables, respectively. In quenched simulations, one can firstly determine γ_G^* independently of γ_F , and then tune γ_F^* for fixed γ_G^* . In contrast, γ_G and γ_F need to be tuned simultaneously in dynamical simulations.

In this work, we use the values of the gauge parameters β and γ_G whose renormalized anisotropy, ξ_G , has been determined in good accuracy. The values of the parameters used will be described in detail in Sec. 4.1. For the quark field, we employ the following two calibration schemes accordingly to the definitions of fermionic anisotropy ξ_F .

- *Mass ratio scheme:* In this scheme, ξ_F is defined as the ratio of meson masses in the temporal and spatial directions,⁴⁾

$$\xi_F^{(M)} \equiv m_H^{(z)} / m_H^{(t)}. \quad (3.1)$$

We use only the pseudoscalar channel as already noted in the previous section for the statistical reason.

- *Dispersion relation scheme:* An alternative definition of ξ_F makes use of the meson dispersion relation,⁹⁾

$$E^2(\vec{p}) = m_H^2 + \vec{p}^2 / (\xi_F^{(DR)})^2. \quad (3.2)$$

$E(\vec{p})$ and m_H are in temporal lattice units and \vec{p} is in spatial lattice units, and hence ξ_F appears. On a finite volume lattice, $p_i = 2\pi n_i / L_i$ ($i = 1, 2, 3$), where L_i is the lattice size in the i -th direction. Eq. (3.2) requires that the rest mass equals the kinetic mass.

3.2. Free quark case

The mass dependences of $\xi_F^{(M)}$ and $\xi_F^{(DR)}$ for the free quark propagator give us a guide to analyze the results of the numerical simulation. The free quark propagator of the staggered quark field (2.7) in the momentum space is²¹⁾

$$S_{\rho\rho'}(p) = \frac{-i \sum_j \Gamma_{\rho\rho'}^j(p) \sin(p_j/2) - i \Gamma_{\rho\rho'}^4(p) \gamma_F \sin(p_4/2) + m_q \delta_{\rho\rho'}}{\sum_j \sin^2(p_j/2) + \gamma_F^2 \sin^2(p_4/2) + m_q^2}, \quad (3.3)$$

where

$$\Gamma_{\rho\rho'}^\mu(p) = e^{ip(\rho-\rho')/2} [\delta_{\rho+\hat{\mu},\rho'} + \delta_{\rho-\hat{\mu},\rho'}] \eta_\mu(\rho). \quad (3.4)$$

The propagator in the t -direction,

$$S_{\rho\rho'}(\vec{p}, t) = \int_{-\pi}^{\pi} \frac{dp_4}{2\pi} e^{ip_4 t} S(p), \quad (3.5)$$

has asymptotic behavior $S_{\rho\rho'}(\vec{p}, t) \propto e^{-E^{(4)}(\vec{p})t}$, with $E^{(4)}(\vec{p})$ implicitly given by

$$\text{ch} E^{(4)}(\vec{p}) = 1 + \frac{2}{\gamma_F^2} \left[\sum_{j=1}^3 \sin^2 \frac{p_j}{2} + m_q^2 \right]. \quad (3.6)$$

Similarly, for the propagator in z -directions,

$$\text{ch} E^{(3)}(\vec{p}) = 1 + 2 \left[\sum_{j=1,2} \sin^2 \frac{p_j}{2} + \gamma_F^2 \sin^2 \frac{p_4}{2} + m_q^2 \right], \quad (3.7)$$

Table I. The lattice parameters. The values of γ_G are based on the results of Ref. ²⁹⁾ ($\beta = 5.95$, 6.10) and Ref. ³⁰⁾ ($\beta = 5.75$). The lattice scale a_σ^{-1} is set by the hadronic radius r_0 . ^{30), 32)} The mean-field values are from Ref. ³²⁾ *Note that those values at $\beta = 5.75$ were evaluated at slightly different anisotropy, $\gamma_G = 3.072$.

β	γ_G	Size	N_{conf}	r_0	$a_\sigma^{-1}(GeV)$	u_σ	u_τ
5.75	3.136	$12^2 \times 24 \times 96$	224	2.786(15)	1.100(6)	0.7620(2)*	0.9871*
5.95	3.1586	$16^2 \times 32 \times 128$	200	4.110(23)	1.623(9)	0.7917(1)	0.9891
6.10	3.2108	$20^2 \times 40 \times 160$	200	5.140(32)	2.030(13)	0.8059(1)	0.9901

where $\vec{p} = (p_1, p_2, p_4)$. For a small quark mass, the rest masses, $M_1 \equiv E(\vec{p} = 0)$, are represented as

$$\begin{aligned} M_1^{(4)} &= \frac{2}{\gamma_F} m_q - \frac{1}{3\gamma_F^3} m_q^3 + O(m_q^4) \\ M_1^{(3)} &= 2m_q - \frac{1}{3} m_q^3 + O(m_q^4). \end{aligned} \quad (3.8)$$

Requiring $\xi_F^{(M)} \equiv M_1^{(3)}/M_1^{(4)} = \xi$,

$$\gamma_F^{*(M)} = \xi \left[1 + \frac{1}{6} \left(1 - \frac{1}{\xi^2} \right) m_q^2 + O(m_q^3) \right] \quad (3.9)$$

By differentiating Eq. (3.6) by p_i , the tuned anisotropy in the dispersion relation scheme is obtained as

$$\gamma_F^{*(DR)} = \xi \left[1 - \frac{1}{3\gamma_F^2} m_q^2 + O(m_q^4) \right]. \quad (3.10)$$

Therefore in both the schemes the quark mass dependences of γ_F^* are of $O(m_q^2)$. As the bare quark mass increases, $\gamma_F^{*(M)}$ increases while $\gamma_F^{*(DR)}$ decreases. These results are useful to understand the results of the numerical simulation.

§4. Numerical result of calibration

4.1. Lattice setup

For the quenched anisotropic lattices, several results for the calibration of gauge field are available. ^{26)–30)} We adopt three sets of the lattice parameters (β, γ_G) at the renormalized anisotropy $\xi = 4$, according to Refs. ^{29), 30)} The parameters are summarized in Table I. These lattices have almost same physical volume. The temporal direction is chosen as the fine direction, and the size in the z -direction is set being the same physical length as the t -direction. The lattice scales are set by the hadronic radius r_0 . ³¹⁾

For the larger two values of β , we adopt the Klassen's result for γ_G^* which was determined within 1% statistical accuracy. ²⁹⁾ These two lattices are almost the same as those used in Ref., ³²⁾ while the size in the z -direction is doubled.

At $\beta = 5.75$, we use a recent result of a precision calibration using the hadronic radius r_0 ³¹⁾ as a calibration condition. ³⁰⁾ With the Lüscher-Weisz noise reduction

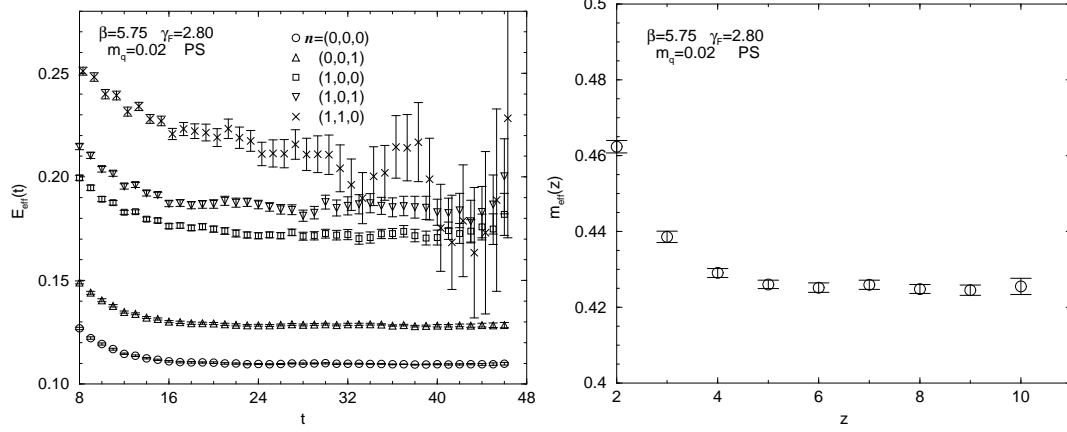


Fig. 1. The effective mass plots for $m_q = 0.02$ and $\gamma_F = 2.8$ at $\beta = 5.75$. The left and right panels show the effective masses in the t - (fine) and z - (coarse) directions, respectively.

technique,³³⁾ the static quark potential was computed to the level of 0.2% accuracy in the fine and coarse directions. Since the value used in this paper was obtained in an earlier stage of the work,³⁰⁾ γ_G^* is slightly different from the final result quoted in Ref.³⁰⁾

We also quote the spatial and temporal mean-field values,³⁴⁾ u_σ and u_τ respectively, in the Landau gauge determined in Ref.³²⁾ For $\beta = 5.75$, the values listed in Table I are not correct exactly, since they were determined at the different γ_G ($\gamma_G = 3.072$). This is not a serious problem, since we quote these values just for a qualitative comparison of the numerical result of γ_F^* with a mean-field estimate, $\gamma_F^{*(MF)} = \xi \cdot (u_\tau/u_\sigma)$.

4.2. Correlator data

In the calibration, we use the pseudoscalar meson correlators with the point source. To perform the calibration along the two schemes described in Sec. 3, we need the following two types of correlators for each set of m_q and γ_F :

- Correlators in the fine (t -) direction at finite momenta. We compute them at momenta $p_i = 2\pi n_i/L_i$ ($i = x, y, z$) where $\vec{n} = (0,0,0)$, $(0,0,1)$, $(0,0,2)$, $(1,0,0)$, $(1,0,1)$, $(1,1,0)$, and $(1,1,1)$. Note that $L_x = L_y = L_z/2$.
- Correlators in the coarse (z -) direction at zero momentum.

To observe whether the correlator is dominated by a single state and to determine a fit range, we observe an effective mass m_{eff} which is defined through

$$\frac{M(t+2)}{M(t)} = \frac{\exp[-m_{eff}(t+2)] + \exp[-m_{eff}(N_t - t - 2)]}{\exp[-m_{eff}t] + \exp[-m_{eff}(N_t - t)]}. \quad (4.1)$$

The definition with lattice spacing $2a$ is adopted since the correlators are composed of monotonously and oscillatingly decaying modes. An effective mass in z -direction is defined similarly. Figure 1 displays the effective masses in the t - and z -directions at $\beta = 5.75$, $m_q = 0.02$, and $\gamma_F = 2.80$.

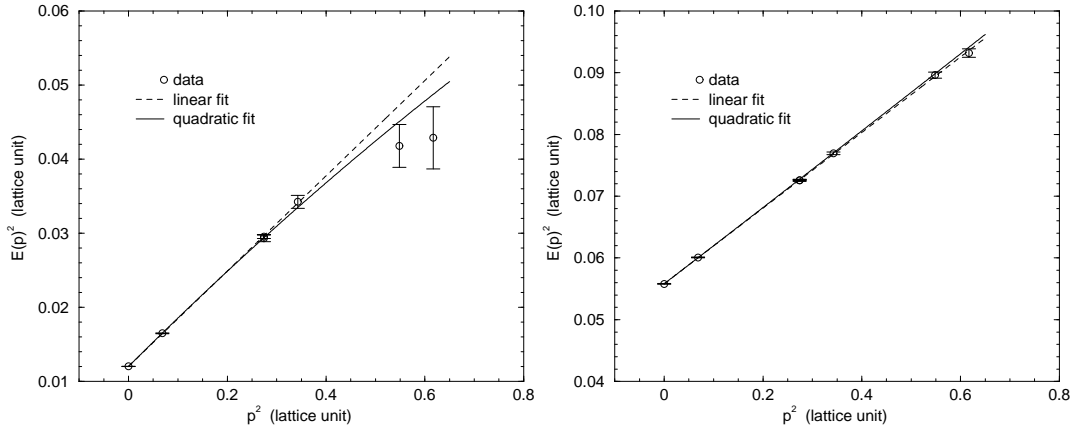


Fig. 2. The dispersion relation at $\beta = 5.75$. The left and right panels display the results at $(m_q, \gamma_F) = (0.02, 2.8)$ and $(0.10, 2.878)$, respectively.

Figure 1 shows that around $t = 24$ and $z = 6$ the correlators reach plateaus where the contribution from the oscillating modes and excited states is sufficiently reduced. We choose a fit range for each quark mass, while the same fit range is used for all the momenta, and fit the correlators to a single exponential form.

Taking the ratio of the masses observed in the t - and z -directions, the fermionic anisotropy $\xi_F^{(M)}$ is determined for each input γ_F .

Figure 2 shows the meson dispersion relation for two quark masses at $\beta = 5.75$. $E(p)^2$ is almost a linear function of p^2 for small momenta, and well fitted to a quadratic form in the whole measured momentum region. The same tendency is observed for all the quark masses and β 's explored. We apply a linear fit to the data of $E(p)^2$ with the smallest five momenta, and determine the fermionic anisotropy $\xi_F^{(DR)}$ through its slope. As displayed in Fig. 2, the linear and quadratic fits give almost the same results, while the former gives a smaller statistical error.

4.3. Determination of γ_F^*

We observe the fermionic anisotropies $\xi_F^{(M)}$ and $\xi_F^{(DR)}$ for several values of γ_F at each quark mass. Figure 3 displays typical γ_F dependences of ξ_F 's at $\beta = 5.75$. This figure shows that the renormalized anisotropy is well represented as a linear function of the bare anisotropy around $\xi_F = \xi$. At $\beta = 5.95$ and 6.10 , we therefore in most cases measure the correlators for two values of γ_F at each quark mass.

Interpolating $\xi_F(\gamma_F)$ linearly in γ_F to $\xi = 4$, we can define a tuned anisotropy parameter γ_F^* . To specify the tuning procedure, the γ_F^* tuned with the mass ratio (dispersion relation) scheme is denoted by $\gamma_F^{*(M)}$ ($\gamma_F^{*(DR)}$). The result of the interpolation is summarized in Table II and displayed in Figure 4.

Figure 4 shows large discrepancies between the results of two calibration schemes in the large quark mass region. The differences remain at the massless limit for $\beta = 5.75$ and 5.95 , while disappears within errors at $\beta = 6.10$. This implies that the discrepancy is due to the finite lattice spacing artifacts. The analysis of the free

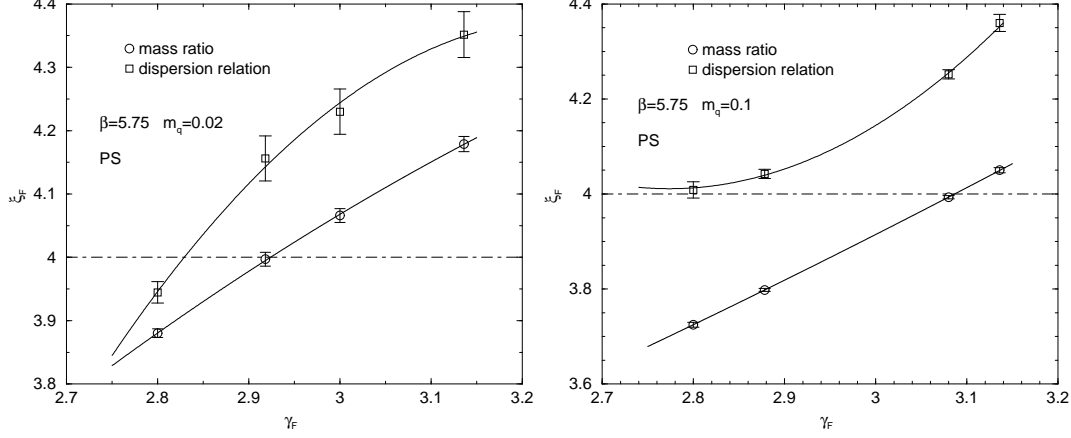


Fig. 3. The dependences of ξ_F 's on γ_F at $\beta = 5.75$. The left and right panels are for $m_q = 0.02$ and 0.10 , respectively. The solid lines are the results of quadratic fits just for a guide of eye, while in the determination of γ_F^* the linear fits using the data of ξ_F near ξ are used.

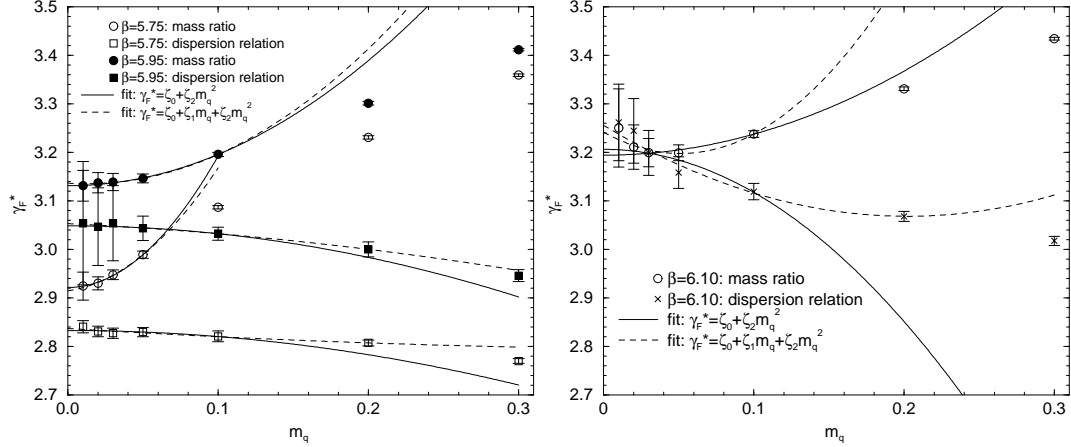


Fig. 4. The results of the calibration. The left panel displays the results at $\beta = 5.75$ and $\beta = 5.95$. The right panel shows the results at $\beta = 6.10$. The data are from Table II. The solid and dashed lines represent the results of fits which are listed in Table III.

quark propagator suggests that the quark mass dependence of γ_F^* on m_q starts with a quadratic term near the chiral limit in both the schemes. This tendency is observed in the dispersion relation scheme more clearly than the mass ratio scheme. As the bare quark mass increases, $\gamma_F^{*(M)}$ increases while $\gamma_F^{*(DR)}$ decreases. These quark mass dependences are consistent with the results for the free quark case, Eqs. (3-9) and (3-10). For $\xi = 4$, these expressions expect larger quark mass dependence for $\gamma_F^{*(M)}$ than $\gamma_F^{*(DR)}$, which is also observed in the numerical result.

The discrepancy between $\gamma_F^{*(M)}$ and $\gamma_F^{*(DR)}$ at the chiral limit can be explained by the $O(a_\sigma^2)$ finite lattice artifacts, such as the flavor symmetry breaking effect, the $O((ap)^2)$ uncertainty in the dispersion relation scheme, and so on. The latter effect

Table II. The results of the calibration. $\gamma_F^{*(M)}$ and $\gamma_F^{*(DR)}$ represent the tuned anisotropy parameters in the mass ratio and dispersion relation schemes, respectively. The pseudoscalar quark masses at γ_F^* are determined by interpolation.

m_q	input γ_F	$\gamma_F^{*(M)}$	$m_{PS}^{(t)}(\gamma_F^{*(M)})$	$\gamma_F^{*(DR)}$	$m_{PS}^{(t)}(\gamma_F^{*(DR)})$
$\beta = 5.75$					
0.50	3.578, 3.5761, 3.136, 2.80	3.5822(21)	0.46494(17)	2.6777(47)	0.59849(73)
0.40	3.471, 3.466, 3.136, 2.778	3.4735(23)	0.42055(17)	2.7239(45)	0.51765(61)
0.30	4.00, 3.353, 3.30, 2.80	3.3590(27)	0.36962(17)	2.7700(47)	0.43311(49)
0.20	3.219, 3.136, 2.80	3.2308(35)	0.30798(19)	2.8073(60)	0.34376(50)
0.10	3.136, 3.08, 2.878, 2.80	3.0870(34)	0.22486(16)	2.821(11)	0.2398(10)
0.05	3.136, 3.00, 2.987, 2.80	2.9891(76)	0.16339(18)	2.8296(95)	0.16979(37)
0.03	3.136, 3.00, 2.948, 2.80	2.947(10)	0.12867(21)	2.827(10)	0.13254(33)
0.02	3.136, 3.00, 2.918, 2.80	2.930(13)	0.10630(22)	2.831(10)	0.10845(29)
0.01	3.136, 3.00, 2.888, 2.80	2.924(28)	0.07620(36)	2.840(12)	0.07765(23)
$\beta = 5.95$					
0.50	3.624, 3.578	3.6246(16)	0.45727(13)	2.8513(94)	0.54393(98)
0.40	3.521, 3.471	3.5198(19)	0.41144(14)	2.897(10)	0.47370(98)
0.30	3.413, 3.353	3.4113(25)	0.35813(15)	2.945(12)	0.39781(99)
0.20	3.292, 3.219	3.3012(36)	0.29292(17)	3.000(15)	0.31307(97)
0.10	3.166, 3.080	3.1958(41)	0.20575(12)	3.032(13)	0.21278(53)
0.05	3.112, 2.987	3.1460(91)	0.14498(18)	3.043(25)	0.14781(65)
0.03	3.170, 3.100	3.139(17)	0.11279(28)	3.053(77)	0.1144(13)
0.02	3.100, 2.918	3.137(20)	0.09258(27)	3.046(80)	0.0940(11)
0.01	3.150, 3.100	3.131(31)	0.06631(27)	3.05(12)	0.0670(11)
$\beta = 6.10$					
0.30	3.21, 3.11	3.4341(26)	0.34436(17)	3.0174(95)	0.38259(96)
0.20	3.21, 3.11	3.3309(35)	0.27754(16)	3.068(10)	0.29493(74)
0.10	3.21, 3.11	3.2377(69)	0.18959(19)	3.119(16)	0.19413(62)
0.05	3.21, 3.16, 3.10	3.199(16)	0.13037(24)	3.158(32)	0.13129(71)
0.03	3.31, 3.21, 3.16	3.199(29)	0.10009(25)	3.198(46)	0.10010(83)
0.02	3.31, 3.21, 3.16	3.210(45)	0.08155(29)	3.244(66)	0.08113(95)
0.01	3.31, 3.21, 3.16	3.250(80)	0.05798(34)	3.261(78)	0.05789(68)

concerns the assumed form of the meson dispersion relation as well as the fitting form for the energies at finite momenta. For the measurement of the mass in the z -direction, the meson quantum number is composed of the staggered quark fields on asymmetric cubes in a z -plane. This leads to a different manifestation of the flavor symmetry breaking effect from that of the mass in t -direction. Although all these effects must disappear toward the continuum limit, at finite lattice spacings they may cause intricate systematic effects.

We determine γ_F^* 's at the vanishing quark mass by fitting the data to a linear form in m_q^2 or quadratic form in m_q ,

$$\gamma_F^* = \zeta_0 + \zeta_1 m_q + \zeta_2 m_q^2, \quad (4.2)$$

where ζ_1 is set to zero in the linear fit. The numbers of data used in the fits are selected appropriately. The result of the fit is listed in Table III, and displayed in Fig. 4. For both the schemes, the linear form in m_q^2 seems to represent well the data in the light quark mass region. Although the quadratic form does not seem to work

Table III. The result of the fits of the tuned anisotropy parameter γ_F^* to the form (4.2). In the case of linear fit, ζ_1 is set to zero. In the second column, ‘M’ and ‘DR’ represent the mass ratio and dispersion relation schemes, respectively. N_{data} is the number of data points used in the fit.

β	mass ratio		N_{data}	dispersion relation			χ^2
	scheme	fit		ζ_0	ζ_1	ζ_2	
5.75	M	linear	4	2.940(11)	-	14.7(11)	0.092
	M	quadratic	4	2.915(42)	0.4(19)	21.(23)	0.001
	DR	linear	5	2.833(10)	-	-1.2(12)	0.013
	DR	quadratic	6	2.837(13)	-0.19(29)	0.2(12)	0.009
5.95	M	linear	5	3.131(14)	-	6.4(12)	0.0007
	M	quadratic	5	3.137(40)	-0.2(12)	7.9(78)	0.0006
	DR	linear	5	3.049(38)	-	-1.6(35)	0.0002
	DR	quadratic	6	3.053(71)	-0.2(11)	-0.6(38)	0.0002
6.10	M	linear	5	3.194(28)	-	4.3(24)	0.008
	M	quadratic	5	3.242(81)	-1.7(21)	17.(13)	0.002
	DR	linear	5	3.206(45)	-	-8.9(40)	0.021
	DR	quadratic	6	3.256(69)	-1.9(10)	4.6(34)	0.007

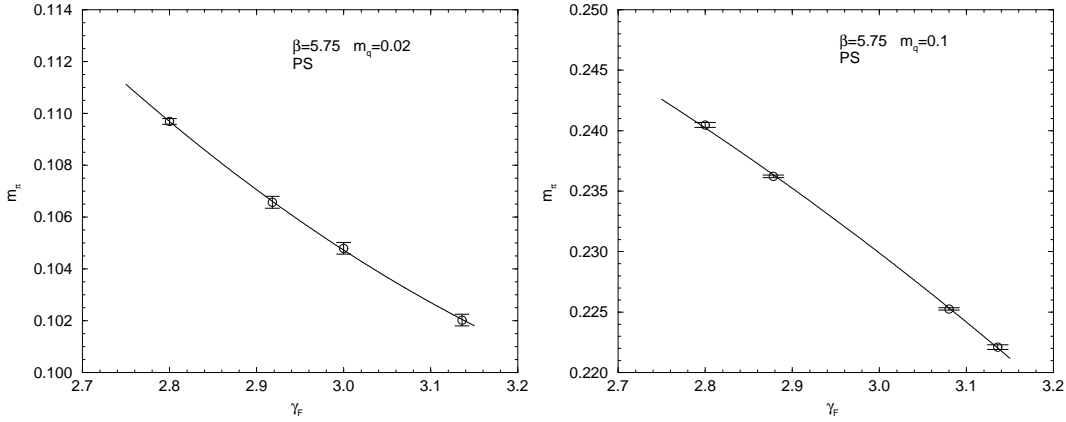


Fig. 5. The dependence of m_{PS} on γ_F at $\beta = 5.75$. The left and right panels show the results at $m_q = 0.02$ and 0.10 , respectively. The solid lines represent the results of quadratic fits.

properly, the γ_F^* at the chiral limit is close to the result of the linear fit.

4.4. Pion mass and the chiral limit

Here we verify that the pseudoscalar meson mass satisfies the PCAC relation with the calibrated anisotropy parameter. Firstly we need to interpolate the pseudoscalar meson mass to $\gamma_F = \gamma_F^*$. Figure 6 shows typical γ_F dependences of PS meson masses at $\beta = 5.75$. The PS meson mass is well represented by a linear form in the vicinity of γ_F^* . The result of the linear interpolation is listed in Table II.

Figure 6 displays the m_q dependence of the pseudoscalar meson mass squared. The proportionality of m_{PS}^2 to m_q well holds for both the calibration schemes. This is also verified by linear fits whose results are listed in Table IV. In either scheme, the intercept is quite small and becomes consistent with zero within the error as β increases. The difference between the two schemes also decreases toward the

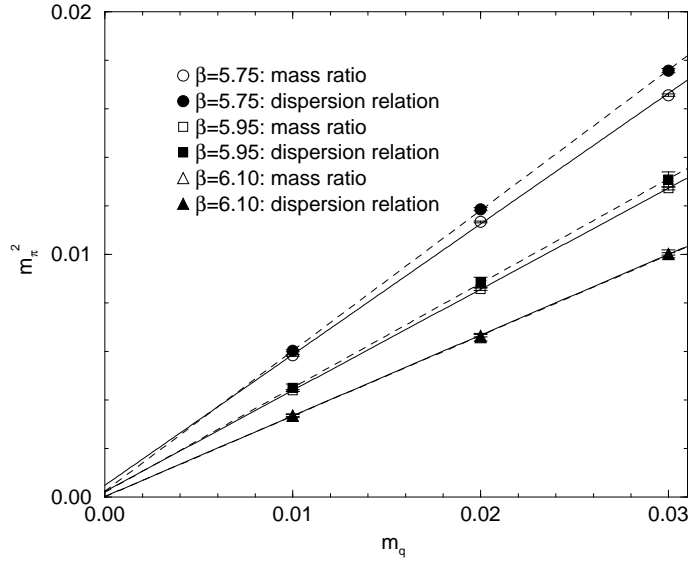


Fig. 6. The dependence of m_{PS}^2 on the bare quark mass m_q . The solid and dashed lines represent the results of linear fits.

Table IV. The results of linear fits of m_{PS}^2 in m_q at the tuned anisotropy γ_F^* .

β	mass ratio			dispersion relation		
	$m_\pi^2(0)$	dm_π^2/dm_q	χ^2	$m_\pi^2(0)$	dm_π^2/dm_q	χ^2
5.75	0.000493(38)	0.5382(17)	8.14	0.000251(49)	0.5784(36)	0.535
5.95	0.000236(36)	0.4164(22)	0.0407	0.00021(20)	0.430(13)	0.0214
6.10	0.000028(43)	0.3325(16)	0.458	0.000025(91)	0.3317(70)	0.319

continuum limit.

4.5. Summary of calibration

In the next section, we investigate the meson spectrum of the anisotropic staggered quark. For this purpose, it is convenient to select one of the results of calibrations as our main result for γ_F^* and compute the spectrum with this value. The differences with the other choices are treated as a systematic uncertainty whose effect on the spectrum should be investigated.

As such a representative, we adopt the γ_F^* in the massless limit determined by the linear fit in m_q^2 in the dispersion relation scheme for the following reasons: As apparent in Fig. 4, $\gamma_F^{*(DR)}$ less depends on the quark mass than $\gamma_F^{*(M)}$. In the light quark mass region we can use the value of γ_F^* at the chiral limit instead of the direct results on those quark masses. The statistical error of the former can be reduced less than those of the latter.

Estimate of the statistical error of γ_F^* at massless limit is provided by the statistical error of the fit result for ζ_0 . On the other hand, the discrepancy between the two calibration schemes gives a typical size of the systematic uncertainty.

To summarize, we select the following values as a representative result of the

calibration:

$$\begin{aligned}\beta = 5.75 : \gamma_F^* &= 2.83(1)(11), \\ \beta = 5.95 : \gamma_F^* &= 3.05(4)(11), \\ \beta = 6.10 : \gamma_F^* &= 3.21(5)(5),\end{aligned}\tag{4.3}$$

where the first and second parentheses denote the statistical and systematic errors, respectively. The latter does not include the quark mass dependence of γ_F^* . At $\beta = 6.10$, the domination of the statistical error around the chiral limit disable us from estimating the systematic error in the same way as other β 's. From the conservative point of view, we substitute the statistical error for the systematic one, since the latter is at most of the same size as the former.

Finally let us compare the result of calibration with the mean-field estimate.³⁴⁾ The mean-field improvement is performed by replacing the link variables as $U_i \rightarrow U_i/u_\sigma$ ($i = 1, 2, 3$) and $U_4 \rightarrow U_4/u_\tau$. The mean-field estimate of γ_F^* in the chiral limit results in

$$\gamma_F^{*(MF)} = \xi \cdot (u_\sigma/u_\tau).\tag{4.4}$$

From the values quoted in Table I, $\gamma_F^{*(MF)}$ is determined as $3.0878(8)^*$ ($\beta = 5.75$), $3.2017(4)$ ($\beta = 5.95$), and $3.2558(4)$ ($\beta = 6.10$). The result of numerical simulation approaches to the mean-field estimate from below as β increases. This suggests that the mean-field value of γ_F^* provides a good guide in the calibration. This feature is helpful in the calibration of anisotropic lattices with dynamical quarks.

§5. Spectroscopy on anisotropic lattices

In this section, we compute the meson spectrum using the anisotropic staggered quark action tuned in the previous section. As noted at the end of Sec. 4, we use the values of γ_F^* quoted in Eq.(4.3) in the simulation and investigate how the uncertainties in γ_F^* affect the spectrum. In practice, we compute the masses at two γ_F 's and linearly interpolate them to γ_F^* in Eq.(4.3). Simultaneously the response of the mass to the change of γ_F is obtained.

The numerical simulation is performed at the same three β 's as in the calibration. At $\beta = 5.75$, the lattice size is the same as in the calibration. At $\beta = 5.95$ and 6.10 , we use the lattices with half size in the z -direction, which were used in Ref.³²⁾ The numbers of configurations are 224, 400, and 200 for $\beta = 5.75$, 5.95 , and 6.10 , respectively.

We measure the meson correlators with the wall source.²⁵⁾ The correlators measured were described in Sec. 2. The gauge configurations are fixed to the Coulomb gauge.

The complication in analyzing the spectrum of the staggered mesons arises from the oscillating modes contained in the correlators. This makes fit more involved than other quark formulations. In extracting the meson masses, we apply the constrained

*) At $\beta = 5.75$ the value has additional systematic error since the mean-field values are obtained at slightly different γ_F .

Table V. The meson spectra from the correlators with the wall source. The meson masses at $m_q = 0$ are determined by linear fits using the data at lightest three m_q 's.

m_q	π	$\tilde{\pi}$	π_3	$\tilde{\pi}_3$	ρ_6^A	ρ_6^B
$\beta = 5.75$						
0.10	0.23846(10)	0.24874(12)	0.29410(40)	0.29494(48)	0.34139(83)	0.3413(13)
0.05	0.16935(12)	0.17916(32)	0.22577(43)	0.22749(69)	0.28222(94)	0.2831(16)
0.03	0.13211(14)	0.14245(43)	0.19110(39)	0.1941(11)	0.25546(96)	0.2557(16)
0.02	0.10854(15)	0.11997(49)	0.17199(48)	0.1753(16)	0.2408(13)	0.2406(23)
0.01	0.07755(15)	0.09159(60)	0.14948(68)	0.1569(22)	0.2209(22)	0.2207(34)
0.	0.01726(67)	0.0495(15)	0.12387(98)	0.1336(34)	0.2064(28)	0.2054(42)
$\beta = 5.95$						
0.10	0.21169(8)	0.21571(12)	0.23084(17)	0.23136(24)	0.25809(47)	0.25816(63)
0.05	0.14754(10)	0.15056(14)	0.16469(20)	0.16529(37)	0.20203(53)	0.20163(73)
0.03	0.11429(13)	0.11704(17)	0.13182(24)	0.13222(50)	0.17759(74)	0.1767(11)
0.02	0.09380(15)	0.09660(23)	0.11250(28)	0.11296(61)	0.16390(94)	0.1633(17)
0.01	0.06712(13)	0.07062(36)	0.08950(48)	0.0905(14)	0.1468(14)	0.1476(24)
0.	0.01503(60)	0.0250(13)	0.05746(87)	0.0589(27)	0.1330(18)	0.1341(30)
$\beta = 6.10$						
0.10	0.19007(9)	0.19200(10)	0.19945(14)	0.19986(21)	0.21820(28)	0.21745(27)
0.05	0.13006(10)	0.13114(19)	0.13759(25)	0.13820(29)	0.16415(33)	0.16414(34)
0.03	0.09990(10)	0.10070(21)	0.10733(20)	0.10767(34)	0.14073(39)	0.14089(53)
0.02	0.0816(11)	0.08239(22)	0.08985(21)	0.08957(41)	0.12870(47)	0.12837(75)
0.01	0.0584(13)	0.05924(32)	0.06889(20)	0.06910(57)	0.11589(72)	0.1134(13)
0.	0.0112(10)	0.0135(19)	0.03684(47)	0.0360(13)	0.10381(87)	0.1012(16)

curve fitting³⁵⁾ to the fit of the correlator to the form (2.18). In principle the constrained curve fitting enables a fit of correlators to multipole forms with arbitrary number of terms. In practice, however, we find that the multipole fitting does not produce a stable result partially because of the large fluctuations. We therefore fit the data to the form (2.18) in relatively narrow fit range where excited modes are sufficiently reduced according to the observation of the effective mass plot.

The result for the spectrum is listed in Table V. The quoted errors are statistical errors evaluated with jackknife method. The meson masses for the four lightest quark masses are displayed in Figure 7. The figure shows that π and $\tilde{\pi}$, π_3 and $\tilde{\pi}_3$, ρ_6^A and ρ_6^B are respectively degenerate. All pionic channels approach to the masses of π , the Goldstone pion channel, as β increases. This behavior is a signal of flavor symmetry restoration toward the continuum limit. The size of flavor symmetry breaking effect is estimated with the mass of, say, π_3 . Our result of the π_3 mass is the same size as the result of Ref.²⁵⁾ at $\beta = 6.0$ ($a \simeq 2$ GeV) on an isotropic lattice.

To determine the masses at the chiral limit, we fit the lightest three masses in each channel to the following forms:

$$m_\pi^2(m_q) = m_\pi^2(0) + b_\pi m_q \quad (\pi, \tilde{\pi}, \pi_3, \tilde{\pi}_3), \quad (5.1)$$

$$m_\rho(m_q) = m_\rho(0) + b_\rho m_q \quad (\rho_6^A, \rho_6^B). \quad (5.2)$$

The results of the fits are also listed in Table V and shown in Figure 7. The above forms well represent the data. We also perform a fit of meson mass squared to a quadratic form in m_q using the four smallest meson masses in each channel. The

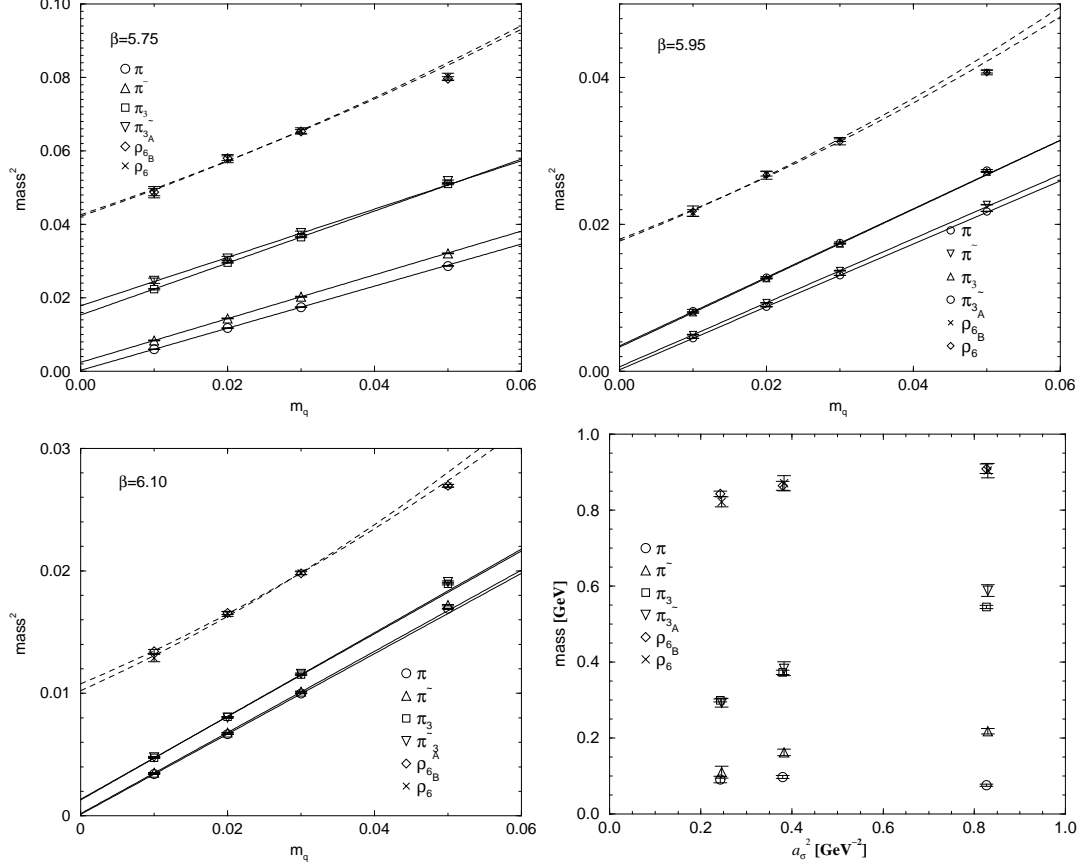


Fig. 7. Meson spectra at $\beta = 5.75$ (top-left), 5.95 (top-right), and 6.10 (bottom-left). The curved lines represent the results of linear fits using the data at the lightest three quark masses. The bottom-right panel shows the meson masses in the chiral limit in physical units.

results of the latter fits are consistent with those with the former linear fits.

In the Goldstone pion channel, a small mass remains even in the chiral limit. This is considered due to the finite volume effect and the uncertainty in γ_F^* . The masses of other pionic channels in the chiral limit decrease as β increases. This behavior is shown more apparently in the bottom-right panel in Figure 7, which displays the meson masses in the chiral limit in physical units as the function of a_σ^2 . Since the staggered action contains $O(a_\sigma^2)$ systematic uncertainty, the flavor symmetry breaking should disappear linearly in a_σ^2 . Our result is consistent with this prediction, while the finite lattice artifact is sizable even at our largest β . Rather large lattice artifact is also expected from the discrepancy between two calibration schemes examined in this work. The ρ meson channel is also consistent with the expected behavior. The masses of ρ in the chiral limit seems to approach the experimental value, $m_\rho = 770$ MeV, within the $O(10\%)$ error of the quenched approximation.

To investigate how the uncertainties of γ_F affect the masses, we evaluate

$$R_H = \frac{(dm_H/d\gamma_F)}{m_H} \quad (5.3)$$

assuming linear dependence of m_H in γ_F in the vicinity of γ_F^* . The subscript H specifies the channel. As a general tendency, R increases as quark mass decreases. This means that the accurate determination of γ_F^* becomes increasingly important as quark mass decreases. R is in general negative. In pionic channels the absolute values of R are 1–2 at $\beta = 5.75$ and 5.95 and around 1 at $\beta = 6.10$ for $m_q = 0.01$, while at $m_q = 0.1$ it decreases less than half the values at $m_q = 0.01$. By adding the two errors in Eq. (4.3) in quadrature, the error of γ_F^* is evaluated as 0.11, 0.12, and 0.07 for $\beta = 5.75$, 5.95, and 6.10, respectively. At $m_q = 0.01$ therefore the uncertainty in the meson mass due to the uncertainty in γ_F^* amounts to 20% at $\beta = 5.75$ and 5.95, and 7% at $\beta = 6.10$. These uncertainties explain the nonvanishing masses of Goldstone pion at the chiral limit. For the vector channels, the values of R are about 1.5 times larger than the pionic channels. These quite significant effects call for precise calibrations in order to use the anisotropic staggered quark action in practical simulations.

§6. Conclusion

In this paper, we performed a calibration of the staggered quark action on quenched anisotropic lattices with the renormalized anisotropy $\xi = 4$. As the calibration procedures, we adopted two schemes which define the fermionic anisotropy through the masses in the fine and coarse directions, and through the meson dispersion relation. At values of β explored in this work, these two schemes produce inconsistent result even in the chiral limit except for our highest β ($a_\sigma \simeq 2$ GeV). Although the discrepancy seems to disappear toward the continuum limit, these rather large discrepancy should be regarded as a source of significant systematic uncertainties.

In the second part of this paper, we performed a meson spectroscopy with the wall source using the values of γ_F^* determined in the calibration. The result is consistent with the result on an isotropic lattice.²⁵⁾ Toward the continuum limit, the flavor symmetry breaking effect seems to disappear. However, the uncertainty of γ_F causes severe effect on the meson masses when the quark mass approaches the chiral limit. For precision studies using staggered anisotropic quarks, precise calibration is indispensable.

This work displayed how the staggered quark action is realized on anisotropic lattices in the quenched approximation. Except for the rather large artifact signaled by the discrepancy between the two calibration schemes, no unreasonable result was found. However, there are numbers of subject which should be examined still in the quenched simulations. It is important to study in more detail how the discrepancy between the calibration schemes disappear as one approaches the continuum limit and to quantify the effect on the observables such as the hadron masses and decay constants. The other important subject is to examine how the various chan-

nels behave when they are measured in the coarse direction or boosted into a finite momentum state. These studies are important to investigate the structure of the staggered quark formulation as well as for applications to the calculations for which the fine temporal cutoff is crucial. For intermediate range of lattice cutoffs, development of improved staggered quark action is also important to avoid the large lattice artifact. The results of this paper provide fundamental information for such further studies.

§7. Toward dynamical simulations

In this final section, we discuss what we learn from the quenched results in this work toward the dynamical simulations. Since in dynamical simulations the generation of gauge configurations requires resources, one wants to finish the calibration as quickly as possible. In this sense, the mass ratio scheme is economical since the statistical error in ξ_F is smaller than the dispersion relation scheme. However, larger quark mass dependence of γ_F is inconvenient to survey the global dependence of γ_F^* on β and m_q . In this sense, the dispersion relation scheme has an advantage. There is another advantage in the latter: one needs to have a large extent only in the temporal (fine) direction. The spatial direction can be kept modest size with which the momentum modes are not very large. One can also use the extended source field to reduce the statistical fluctuations. For these reasons, we realize that the dispersion relation scheme is more suitable for the calibration of dynamical lattices.

It is important to forecast γ_G^* and γ_F^* to avoid waste of simulation. The mean-field estimate is helpful for this purpose. At the quenched level, the mean-field value provides a good estimate of the anisotropy parameter of the gauge action. In this work, we showed that the tuned anisotropy γ_F^* approaches to the mean-field value from below as β increases. These may help us to select the values of γ_G and γ_F to be explored.

Our preliminary result of the calibration of dynamical anisotropic lattices with the same combination of actions as in this work indicates that the renormalized anisotropy defined through the gauge observable less depends on γ_F , and one through the fermionic observable less depends on γ_G .³⁶⁾ These dependences of ξ_G and ξ_F on γ_G and γ_F indicate that linear fits may suffice to determine γ_G^* and γ_F^* satisfying $\xi_G(\gamma_G^*, \gamma_F^*) = \xi_F(\gamma_G^*, \gamma_F^*) = \xi$. We would be able to perform the calibration by generating configurations at best at four (or three) sets of (γ_G, γ_F) .

Acknowledgment

We thank A. Nakamura, M. Okawa, and members of QCD-TARO collaboration for useful discussions. The numerical simulation was done on a NEC SX-5 at Research Center for Nuclear Physics, Osaka University, and on a Hitachi SR8000 at High Energy Accelerator Research Organization (KEK). H.M. and T.U. were supported by Japan Society for the Promotion of Science for Young Scientists.

References

- 1) C. Bernard *et al.*, Nucl. Phys. B (Proc. Suppl.) **106** (2002), 199.
- 2) F. Karsch, Nucl. Phys. **B205** (1982), 285.
- 3) Y. Namekawa *et al.* [CP-PACS Collaboration], Phys. Rev. D **64** (2001), 074507.
- 4) Ph. de Forcrand *et al.* [QCD-TARO Collaboration], Phys. Rev. D **63** (2001), 054501.
- 5) T. Umeda, R. Katayama, O. Miyamura and H. Matsufuru, Int. J. Mod. Phys. A **16** (2001), 2215.
- 6) N. Ishii, H. Suganuma, and H. Matsufuru, Phys. Rev. D **66** (2002), 014507; *ibid.* **66** (2002), 094506; N. Ishii and H. Suganuma, hep-lat/0309102.
- 7) T. Umeda, K. Nomura, and H. Matsufuru, hep-lat/0211003, to appear in Eur. Phys. J. C.
- 8) M. Asakawa and T. Hatsuda, hep-lat/0308034.
- 9) T. R. Klassen, Nucl. Phys. B (Proc. Suppl.) **73** (1999), 918.
- 10) P. Chen, Phys. Rev. D **64** (2001), 034509.
- 11) J. Harada, A. S. Kronfeld, H. Matsufuru, N. Nakajima and T. Onogi, Phys. Rev. D **64** (2001), 074501.
- 12) M. Okamoto *et al.* [CP-PACS Collaboration], Phys. Rev. D **65** (2002), 094508.
- 13) J. Harada, H. Matsufuru, T. Onogi and A. Sugita, Phys. Rev. D **66** (2002), 014509.
- 14) C. J. Morningstar and M. J. Peardon, Phys. Rev. D **60** (1999), 034509.
- 15) Y. Nemoto, N. Nakajima, H. Matsufuru and H. Suganuma, Phys. Rev. D **68** (2003), 094505.
- 16) C. Liu, J. h. Zhang, Y. Chen and J. P. Ma, Nucl. Phys. **B624** (2002), 360.
- 17) T. Hashimoto, A. Nakamura and I. O. Stamatescu, Nucl. Phys. **B400**, 267 (1993); Nucl. Phys. **B406**, 325 (1993).
- 18) Y. Nakahara, M. Asakawa and T. Hatsuda, Phys. Rev. D **60**, 091503 (1999); M. Asakawa, T. Hatsuda and Y. Nakahara, Prog. Part. Nucl. Phys. **46**, 459 (2001).
- 19) T. Umeda *et al.* [CP-PACS Collaboration], Phys. Rev. D **68** (2003), 034503.
- 20) L. Levkova *et al.*, Nucl. Phys. B (Proc. Suppl.) **106** (2002), 218.
- 21) See, for example, H. J. Rothe, *LATTICE GAUGE THEORIES: An Introduction*, 2nd ed., World Scientific, Singapore (1997).
- 22) H. Kluberg-Stern, A. Morel, O. Napoly, and B. Petersson, Nucl. Phys. **B220** (1983), 447.
- 23) M. F. L. Golterman, Nucl. Phys. **B273** (1986), 663.
- 24) J. P. Gilchrist, G. Schierholz, H. Schneider, and M. Teper, Nucl. Phys. **B248** (1984), 29.
- 25) R. Gupta, G. Guralnik, G. W. Kilcup and S. R. Sharpe, Phys. Rev. D **43** (1991), 2003.
- 26) G. Burgers, F. Karsch, A. Nakamura and I. O. Stamatescu, Nucl. Phys. **B304** (1988), 587.
- 27) M. Fujisaki *et al.* [QCD-TARO Collaboration], Nucl. Phys. B (Proc. Suppl.) **53** (1997), 426.
- 28) F. Karsch, J. Engels and T. Scheideler, Nucl. Phys. B (Proc. Suppl.) **63** (1998), 427; J. Engels, F. Karsch and T. Scheideler, Nucl. Phys. **B564** (2000), 303.
- 29) T. R. Klassen, Nucl. Phys. **B533** (1998), 557.
- 30) H. Matsufuru, M. Okawa, T. Onogi, and T. Umeda, hep-lat/0312009, to appear in Proceedings of The XXI International Symposium on Lattice Field Theory, Tsukuba, Japan, July 15-19, 2003.
- 31) R. Sommer, Nucl. Phys. **B411** (1994), 839.
- 32) H. Matsufuru, T. Onogi and T. Umeda, Phys. Rev. D **64** (2001), 114503.
- 33) M. Lüscher and P. Weisz, JHEP **0109** (2001), 010.
- 34) G. P. Lepage and P. B. Mackenzie, Phys. Rev. D **48** (1993), 2250.
- 35) G. P. Lepage *et al.*, Nucl. Phys. B (Proc. Suppl.) **106** (2002), 12.
- 36) K. Nomura, T. Umeda, and H. Matsufuru, hep-lat/0312010, to appear in Proceedings of The XXI International Symposium on Lattice Field Theory, Tsukuba, Japan, July 15-19, 2003.